International Tables for X-ray Crystallography (1968). Vol. III, pp. 197–199. Birmingham: Kynoch Press.

International Tables for X-ray Crystallography (1974). Vol. IV, pp. 270–271. Birmingham: Kynoch Press.

LEHMANN, M. S. & WILSON, S. (1977). Internal Report. ILL, Grenoble.

MESS, K. W., LAGENDIJK, E., CURTIS, D. A. & HUISKAMP, W. J. (1967). *Physica (Utrecht)*, **34**, 126–148.

POWELL, H. M. & WELLS, A. F. (1935). *J. Chem. Soc.* pp. 359–362.

SCHOMAKER, V. & TRUEBLOOD, K. N. (1968). *Acta Cryst.* B**24**, 63–76.

STAPELE, R. P. VAN, BELJERS, H. G., BONGERS, P. F. & ZIJLSTRA, H. (1966). *J. Chem. Phys.* **44**, 3719–3725.

STEWART, J. M. (1976). The XRAY 76 system. Tech. Rep. TR-446. Computer Science Center, Univ. of Maryland, College Park, Maryland.

WIELINGA, R. F., BLÖTE, H. W. J., ROEST, J. A. & HUISKAMP, W. J. (1967). *Physica (Utrecht)*, **34**, 223–240.

Acta Cryst. (1980). B**36**, 512–523

Bonding in $[S_2O_6]^{2-}$: Refinement and Pictorial Representation from an X-ray Diffraction Study of $Na_2S_2O_6.2H_2O$ and $Na_2S_2O_6.2D_2O$

BY A. KIRFEL AND G. WILL

Mineralogisches Institut der Universität Bonn, Lehrstuhl für Mineralogie und Kristallographie, Poppelsdorfer Schloss, D-5300 Bonn, Federal Republic of Germany

(*Received* 22 *August* 1979; *accepted* 4 *October* 1979)

Abstract

Conventional refinements of room-temperature data sets for $Na_2S_2O_6.2H_2O$ and $Na_2S_2O_6.2D_2O$ led to $R = 0.0198$ and $R = 0.0229$ respectively. Ensuing difference density syntheses showed significant charge accumulations in the S–S and S–O bonds. Further studies of the electron distribution in the $[S_2O_6]^{2-}$ anion were based on four models, which resulted in significantly improved R values. In the first three models, applicable to conventional least-squares programs, no external constraint was imposed on the anion charge, which was proved to be doubly negative within the limits of tolerance. (*a*) Ionic model: variation of the S and O occupancies ($R = 0.0192/0.0224$). The anion charge was shown to be uniformly distributed on the O atoms, while the S atoms remained unaffected. (*b*) Bond model: conventional refinement plus free point charges initially placed between each pair of bonded atoms ($R = 0.0162/0.0210$). The anion charge was found to be distributed on the seven bonds. (*c*) Core model: as (*b*) but representation of S and O by Ne and He cores respectively. Initially additional free point charges were placed on the atomic positions ($R = 0.0139/0.0191$). The final atomic parameters were used for (X–X) syntheses yielding improved dynamic deformation densities. (*d*) Multipole model: refinement with neutral S and O atoms plus atomic deformation functions ($R = 0.0129/0.0172$). Refined multipole coefficients were used to calculate static deformation densities and their e.s.d.'s. The features of the static deformation densities of both compounds are in good qualitative agreement. Examples of three-dimensional pictorial representations of individual atomic deformation density and total static density distributions are given. All refinement results show $[S_2O_6]^{2-}$ to behave like a charged molecular fragment held together by strong covalent bonds.

Introduction

In a previous paper (Kirfel, Will & Weiss, 1980; hereafter called part I) the crystal structures of $Na_2S_2O_6.2H_2O$ and its deuterated homologue have been reinvestigated and refined by conventional least-squares methods from X-ray diffraction data. As in part I, the compounds are referred to as NAH and NAD respectively. A study of the electron density distribution in the unit cell beyond the configurational analysis of the structure, *i.e.* the study of bond densities, imposes requirements on the data, which are matched only partially in the present work, since both data sets suffer from a limited scattering angle, $2\theta_{max} = 60°$, corresponding to a cut-off at $s = 0.70$ Å^{-1}. This prevents high-order refinements and also excludes some experimental information from the bonding contributions of the core electrons and of charge concentrations in the vicinity of the nuclei-like lone-pair electrons. In spite of these shortcomings, we decided to look more closely at the electron distribution, since the data sets are of good quality and we were interested in testing various refine-

0567-7408/80/030512-12$01.00

ment models for the $[S_2O_6]^{2-}$ anion. The deformation densities of bonded second-row elements such as S have not been studied extensively and accumulation of experimental results seems desirable.

We have confined our interest to the $[S_2O_6]^{2-}$ anion since Na^+, which has a closed-shell electron configuration, does not seem to possess a bond distribution of special interest. Consequently, the charge character of Na has been carried through all subsequent calculations as single positive. The electrons removed from the two Na atoms must be transferred to the S_2O_6 complex and together with the assumption of the predominantly covalent bonding in S_2O_6, corroborated in the conventional refinement (part I), significant deviations of the electron densities from the neutral spherical-atom model were expected. Such deviations should be comparable for both compounds since the substitution of H by D can be regarded as giving rise to no significant changes of the bonding conditions within the S_2O_6 complex.

We have the additional advantage that the two compounds were investigated on two different diffractometers with differently monochromatized Mo $K\alpha$ radiation, and this implies that the results, if comparable, are predominantly biased by the specific properties of the model for each refinement rather than by systematic experimental errors.

Five models were applied to the $[S_2O_6]^{2-}$ anion which we will refer to as follows: (*a*) SAM = conventional neutral spherical-atom model, (*b*) IM = ionic model, (*c*) BM = bond model, (*d*) CM = core model, (*e*) MM = multipole model.

The models were tested for significant improvements of the agreement factors compared to the conventional refinement and for changes of the positional and vibrational parameters. The results are compiled in Tables 9 and 10 in the form of bond distances and a rigid-bond test. According to Hirshfeld (1976), the physical acceptability of the vibrational parameters of the individual atoms in a molecule can be surveyed by comparing the mutual mean-square amplitudes of vibration, $z^2_{A,B}$ and $z^2_{B,A}$, of a pair of bonded atoms in the bond directions. If the molecule behaves like a rigid body, implying that most of the intramolecular modes involve torsional, to a lesser extent angle bending, and a negligible amount of bond-stretching vibrations, $z^2_{A,B} - z^2_{B,A}$ is expected to vanish within the limits of tolerance. Regarding the S_2O_6 arrangement as such a molecular unit, this test may be used as a measure of the extent to which the vibrational parameters are free from bias introduced by the applied model.

The conventional neutral spherical-atom model

The results of the conventional refinement have been given in part I. In addition we list here in Table 10 the result of rigid-bond tests applied to all pairs of bonded atoms of the $[S_2O_6]^{2-}$ anion. Almost all mutual atomic vibrations are equal within the limits of tolerance given by the experimental $\sigma(u^2) = 6 \times 10^{-4}$ Å^2. This is also expressed by the r.m.s. discrepancies of $5{\cdot}4 \times 10^{-4}$ for NAD and $10{\cdot}5 \times 10^{-4}$ Å^2 for NAH. For the latter, only one exceptional z^2 difference was found: for the

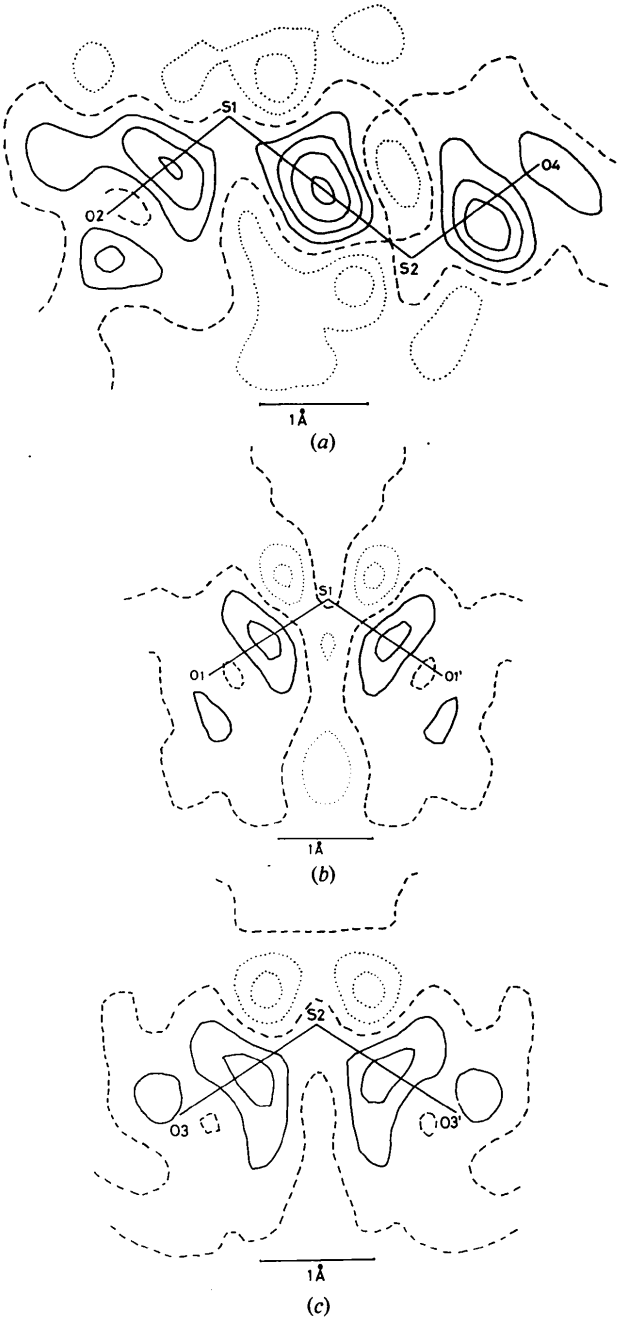

Fig. 1. Dynamic deformation densities in $[S_2O_6]^{2-}$ from conventional refinement of NAH. Contours are at intervals of 0·1 e Å^{-3}, negative contours are dotted, the zero line is broken. (*a*) Mirror plane containing S(1), S(2), O(2), O(4), (*b*) plane O(1), S(1), O(1′), (*c*) plane O(3), S(2), O(3′).

Table 1. *Bond peak heights* (e Å^{-3}) *observed from* $d\rho$ *(SAM) and* $d\rho$ *(CM) and calculated from BM*

	SAM		CM	BM	
	NAH	NAD	NAH	NAH	NAD
S(1)–S(2)	0·43	0·43	0·46	0·67	0·62
S(1)–O(1)	0·23	0·20	0·36	0·65	0·66
S(1)–O(2)	0·30	0·40	0·48	0·70	1·07
S(2)–O(3)	0·25	0·22	0·43	0·72	0·65
S(2)–O(4)	0·39	0·25	0·62	1·01	0·86
⟨S–O⟩	0·28		0·45	0·72	
⟨S–S⟩	0·43		0·46	0·65	

S(2)–O(3) bond. Thus, the test shows all but one of the thermal parameters to be basically unbiased by the model and hence encourages the conclusion that deformation densities calculated from these refinement results should not be falsified, at least qualitatively.

Difference Fourier sections through the planes defined by O(2)–S(1)–S(2)–O(4), O(1)–S(1)–O(1′), and O(3)–S(2)–O(3^{I}) (Fig. 1) show the dynamic difference densities along the bond directions in the anion of NAH. The plots for NAD are very similar. These maps reveal the expected charge accumulations due to covalent bonding at the midpoints of the bonds. The charge transfer within the electron cloud of the S atoms is indicated by the troughs observed opposite each bond angle. There are peaks close to the O atom positions and approximately perpendicular to the bonds, which can be associated with lone-pair electrons. Table 1 gives the peak heights of the bonds of both NAH and NAD obtained from the deformation densities $d\rho$. Treating all S–O bonds as chemically equivalent, we calculate an average peak height of 0·28 e Å^{-3} compared to 0·43 e Å^{-3} for the S–S bond. Similar S–O bond peak heights of about 0·30 e Å^{-3} were found by Bats (1977) in a sulfate group. Of course, the values of Table 1 have to be treated with great care. It is known that series truncation may diminish peak heights considerably (Stevens, 1978) in comparison to the saturation values obtainable for infinite resolution. Since the deformation densities of both compounds suffer equally from the data cut-off, the results have to be regarded as too low and we can merely consider their relative agreement.

The ionic model (IM)

In the conventional refinement S and O were treated as neutral atoms without considering the double negative charge of $[S_2O_6]$ necessary to guarantee the neutrality of the crystal. Under the assumption that the anion is built up from charged atoms, the multiplicities of the S and O atoms were now included in the list of variables. No constraint was imposed on the total anion charge. The refined multiplicities were expected to reflect in first-order approximation the charge character of the individual atoms as well as the distribution of the anion charge.

These refinements of both data sets did not affect significantly the positional and thermal parameters which consequently are not listed. There is a minor improvement in the R values, $R = 0{\cdot}0253$ ($R_{\text{unobs. omitted}} = 0{\cdot}0192$) for NAH and $R = 0{\cdot}0273$ ($R_{\text{u.o.}} = 0{\cdot}0224$) for NAD due to the adjustments of the occupancies. Their values converted to numbers of electrons, Z, are listed in Table 2. Apart from the mutual agreement, the results are interesting in two ways. The charges of the S atoms remained unaffected, indicating neutral S, while the O atom charges increased almost uniformly by 0·32 e on average. The sums of the total excess charges amount to 1·94 (38) e for NAH and 1·89 (38) e for NAD, and thus the twofold negative character of the $[S_2O_6]$ anion is already corroborated without external constraint. This leads to the simple model that the two electrons transferred from the Na atoms are uniformly distributed over the six O atoms while the neutral S atoms are solely involved in covalent bonds. The SAM is modified only marginally, indicating that the classical chemical models employing greater deviations from atomic neutrality, such as S^{4+}, O^{2-}, *etc.*, must be discarded as inadequate (*cf.* Kirfel, Will & Weiss, 1980; Berthold & Weiss, 1967). Consequently, it seems advisable for conventional refinement purposes to treat similar anion complexes such as $[SO_4]^{2-}$ or $[SiO_4]^{2-}$ as neutral-atom arrangements rather than allocate scattering factors derived from chemical considerations (see also Will, Frazer, Shirane & Cox, 1965).

The bond model (BM)

The bond model is based on the SAM augmented by bonding valence electrons initially placed on the midpoints of the interatomic bonds. These charge clouds ($E1$ to $E5$) are represented in the calculations by point scatterers ($f = 1{\cdot}0$) with adjustable multiplicities. Their

Table 2. *Refined occupancies and charges* Z (e) *from IM with e.s.d.'s in parentheses*

	NAH		NAD	
	Occupancy	Z	Occupancy	Z
S(1)	0·500 (2)	16·00 (6)	0·500 (2)	16·00 (6)
S(2)	0·501 (2)	16·03 (6)	0·500 (2)	16·00 (6)
O(1)	1·043 (5)	8·34 (4)	1·039 (5)	8·31 (4)
O(2)	0·515 (3)	8·24 (5)	0·516 (3)	8·27 (5)
O(3)	1·041 (5)	8·33 (4)	1·045 (5)	8·36 (4)
O(4)	0·523 (3)	8·37 (5)	0·516 (3)	8·27 (5)
Total Z		81·94 (38)		81·89 (38)

distributions are described by three-dimensional Gaussian functions including the effects of thermal vibrations. Thus, the model allows a consideration of the covalent-bond charge densities observed in Fig. 1. In this simple augmentation the charge density is separated into two parts expressed in reciprocal space by:

$$F_{\mathbf{h}} = F_{\mathbf{h}}^{\mathrm{SAM}} + \sum_{j=1}^{\mathrm{NB}} n_j^s \exp(2\pi i \mathbf{h} \mathbf{r}_j^s) \exp(-\mathbf{h}^T \beta_j^s \mathbf{h}),$$

where F^{SAM} refers to the neutral atoms and the superscripts s refer to the additional σ-bond charge clouds (NB = number of bonds). Compared to the SAM, this model includes up to 41 additional parameters n^s, x^s, y^s, z^s, β^s. Again, no total anion-charge constraint was considered. The straightforward application of the BM with isotropic (I) and anisotropic (A) temperature factors for the point scatterers on both data sets yielded improved R values (Table 9) showing that this model is better than the SAM beyond the 0·005 significance level.

As a first consequence of the BM, we observe a significant elongation of the S—O distances, on average by 0·008 Å in NAH and by 0·006 Å in NAD (Table 9). The S—S distances remained unaffected. Compared to the bond-distance results of the other models, it is not unreasonable to assume an over-representation of the σ-bond charge clouds which then induces a shift of the center of gravity of the O atom electron distribution away from S.

Table 3 contains the distances and angles between the refined charge-cloud centers and the atoms. The differences of corresponding results of NAH and NAD are well within the sums of the e.s.d.'s. While the charge clouds $E1$ to $E3$ on the mirror plane through the anion remained on the associated bonds, the charges $E4$ and $E5$ were shifted towards the mirror plane as can be seen in Fig. 2 and is also indicated by the mean angles S(1)—$E4$—O(1) = 142 and S(2)—$E5$—O(3) = 131°.

Table 3. *Distances* (Å) *and angles* (°) *for valence electron charge clouds from BM refinement*

	NAH	NAD	Average
S(1)—$E1$	1·04 (12)	1·12 (9)	1·08 (5)
S(2)—$E1$	1·10 (12)	1·02 (9)	1·06 (5)
S(1)—$E2$	0·91 (4)	0·92 (11)	0·91 (3)
S(1)—$E4$	1·06 (4)	1·13 (10)	1·09 (3)
S(2)—$E3$	0·96 (4)	1·06 (7)	1·01 (3)
S(2)—$E5$	1·08 (4)	1·19 (5)	1·13 (3)
O(1)—$E4$	0·46 (3)	0·39 (8)	0·43 (3)
O(2)—$E2$	0·55 (4)	0·54 (11)	0·55 (4)
O(3)—$E5$	0·49 (2)	0·37 (7)	0·43 (2)
O(4)—$E3$	0·50 (4)	0·42 (6)	0·46 (3)
S(1)—$E1$—S(2)	174 (12)	175 (9)	175 (8)
S(1)—$E2$—O(2)	176 (8)	178 (15)	177 (5)
S(2)—$E3$—O(4)	178 (10)	153 (20)	166 (7)
S(1)—$E4$—O(1)	143 (8)	141 (17)	142 (6)
S(2)—$E5$—O(3)	132 (7)	130 (17)	131 (6)

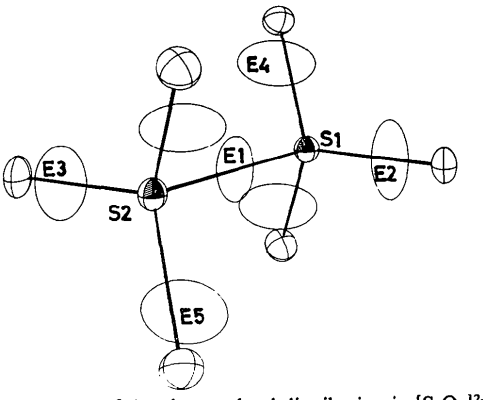

Fig. 2. *ORTEP* plot of the charge-cloud distribution in $[S_2O_6]^{2-}$ of NAH from bond model.

The charge $E1$ stayed at its initial position halfway between the S atoms (S—$E1$ = 1·07 Å), while all other charges were shifted towards the O atoms in accordance with the greater electronegativity of O (3·44) compared to S (2·58). The mean S—E distance in the S—O bonds is 1·04 Å which is equivalent to the covalent single-bond radius of S in tetrahedral coordination (Pauling, 1960). The mean O—E distance, on the other hand, is 0·47 Å which corresponds to the maximum of the radial electron distribution of O calculated by Hartree & Fock.

Results of the charge-cloud distributions are listed in Table 4. Anisotropic temperature factors are omitted since they are highly correlated with the associated occupancies (charges). This can be seen, for example, from refinement (I) where the average values of Z and B for NAH are much greater than those for NAD. The calculated values for the charges on the bonds obtained from the BM do not seem to yield reliable information. However, upon removal of the Z–B correlations, the values display a common physical result. Calculation of

$$p(0) = 4\pi \int_0^{\infty} r^{*2} Z \exp(-Br^{*2}/4)\, \mathrm{d}r^*,$$

$$r^* = 2 \sin\theta/\lambda,$$

gives the peak heights of the charge clouds, which compare well within the limits of tolerance. The average peak heights are 0·65 e Å^{-3} for the S—S bond and 0·72 e Å^{-3} for the S—O bonds. It is interesting to note that reflection sets of two olivine (Fe_2SiO_4) crystals refined with the BM yielded mean peak heights on the Si—O bonds of 0·72 e Å^{-3} and peak to Si distances matching the Si covalent-bond radius (Nover, 1977).

Fig. 2 shows the BM *ORTEP* drawing (Johnson, 1965) produced from the positional and thermal parameters of NAH. The 50% probability ellipsoids represent the atomic vibrations and the σ-bond charge

Table 4. *BM refinement results: numbers of electrons Z of σ-bond charge clouds, associated temperature factors B* (Å²), *and calculated peak heights ρ(0)* (e Å⁻³) (*upper row NAH, lower row NAD*)

			Refinement (I)		Refinement (A)
Charge	Bond	Z	B	$\rho(0)$	Z
$E1$	S(1)–S(2)	0·18 (4)	5·3 (1·5)	0·67 (13)	0·18 (4)
		0·10 (4)	3·9 (1·9)	0·62 (24)	0·12 (4)
$E2$	S(1)–O(2)	0·35 (5)	8·0 (1·5)	0·70 (9)	0·32 (6)
		0·13 (4)	3·0 (1·4)	1·07 (39)	0·20 (6)
$E3$	S(2)–O(4)	0·37 (5)	6·4 (1·1)	1·01 (13)	0·40 (6)
		0·14 (4)	3·8 (1·6)	0·86 (28)	0·16 (4)
$E4$	S(1)–O(1)	0·39 (4)	8·9 (1·3)	0·65 (8)	0·45 (5)
		0·18 (3)	5·3 (1·5)	0·66 (16)	0·20 (3)
$E5$	S(2)–O(3)	0·31 (4)	7·1 (1·1)	0·72 (9)	0·36 (4)
		0·19 (3)	5·5 (1·4)	0·65 (13)	0·24 (4)
Total		2·30 (29)		5·15	2·52 (34)
		1·10 (25)		5·15	1·36 (28)

accumulations, corresponding well with the findings of the dynamic deformation density sections.

The average effect of the BM refinement on the atomic vibrational parameters is for both substances an increase of the r.m.s. (Δz^2) (Table 10). However, the bonds are not affected uniformly, since noticeable Δz^2 differences are only found for the S(1)–O(2) bond in NAH and the S(2)–O(4) bonds in both NAH and NAD. However, a direct correlation of these differences with the parameters of the point charges E is not detectable.

The core model (CM)

As the next step we applied the core model (CM), which can be regarded as a further development of the BM. It is based on the refinement model described by Hellner (1977) and has been tested, for example, on diborane (Mullen & Hellner, 1977) and cyanuric acid (Kutoglu & Hellner, 1978). In this work, however, no separate point charges associated with lone-pair electrons were considered. In reciprocal space the superposition of the charge density is expressed by three terms:

$$F_{\mathbf{h}} = \sum_{j=1}^{N} f_j^c \exp(2\pi i \mathbf{h} \mathbf{r}_j^c) \exp(-\mathbf{h}^T \beta_j^c \mathbf{h}) + \sum_{j=1}^{N} n_j^v \exp(2\pi i \mathbf{h} \mathbf{r}_j^v) \exp(-\mathbf{h}^T \beta_j^v \mathbf{h}) + \sum_{j=1}^{NB} n_j^s \exp(2\pi i \mathbf{h} \mathbf{r}_j^s) \exp(-\mathbf{h}^T \beta_j^s \mathbf{h}).$$

Superscripts c refer to the atomic cores with f_c as the scattering factors of the He core for O and of the Ne core for S (*International Tables for X-ray Crystallography*, 1974). The valence electron clouds around and the charge accumulations between the atoms are again represented by point scatterers ($f = 1{\cdot}0$) with adjustable multiplicities and temperature factors. As for the BM, superscript s refers to the charges associated with σ bonds between the atoms, while v refers to the valence shells centered initially on the atomic positions. The results of the refinement without charge constraint, agreement factors, interatomic distances, and mutual thermal vibrations are listed in Tables 9 and 10. The new model yielded a considerable decrease in the R values, which according to a Hamilton test is not merely due to the increased number of variables. Fig. 3 shows an *ORTEP* drawing of the refined cores and

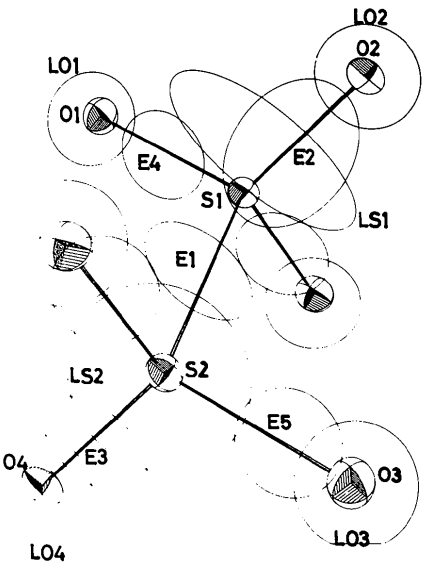

Fig. 3. *ORTEP* plot of the charge-cloud distribution in $[S_2O_6]^{2-}$ of NAH from core model. Atomic ellipsoids represent core vibrations.

Table 5. *Valence electron charge distribution in* $[S_2O_6]^{2}$ *from core-model refinement* (*anisotropic temperature factors*)

	NAH Z (e)	NAD Z (e)	Weighted mean Z (e)
LS1	1·5 (4)	1·8 (6)	1·6 (2)
LS2	3·9 (6)	3·5 (6)	3·7 (3)
LO1	4·8 (7)	6·3 (1)	5·9 (1)
LO2	5·4 (3)	4·6 (5)	5·1 (2)
LO3	5·0 (2)	5·9 (4)	5·3 (1)
LO4	5·2 (5)	4·2 (8)	4·8 (3)
$E1$	1·2 (5)	1·1 (5)	1·2 (3)
$E2$	2·6 (5)	2·2 (7)	2·4 (3)
$E3$	0·8 (4)	3·7 (7)	1·8 (3)
$E4$	2·2 (7)	1·0 (2)	1·2 (2)
$E5$	2·4 (2)	1·3 (4)	2·1 (1)
Total	49·51	49·76	49·79
S_2O_6	81·51	81·76	81·79

charge clouds for NAH. The atomic ellipsoids represent the thermal vibrations of the cores, *i.e.* the *K*- and *L*-shell electrons, while the simple open ellipsoids indicate the sizes and positions of the valence electron and σ-bond electron clouds. Table 5 contains the number of electrons associated with the individual charge clouds for both substances together with their weighted mean values. There are no systematic differences detectable between the refinements. It is surprising to find differences between the S(1) and S(2) valence clouds, which can be regarded as an indication for slightly different electronic states of the S atoms.

A successful refinement with the CM implies that the final positional and thermal parameters of the cores reflect atomic parameters without undesired bias from bonding effects. If this is true, the method should be equivalent to the widely applied high-order refinement technique and could be used for the evaluation of less biased parameters from restricted data sets such as the present ones. Fig. 4 shows examples of the dynamic deformation densities corresponding to those in Fig. 1 calculated by *X*–*X* syntheses, in which the core parameters were used for the calculation of ρ_c. According to Kutoglu & Scheringer (1979) these sections can be called *X*–*X* ($1s^2$,$1s^22s^2$ core) maps. The authors conclude from their own experiences and earlier investigations (Coppens, 1971; Stevens & Hope, 1975) that the core refinement technique can well produce reliable results, at least for unpolarized atoms. In fact, qualitatively the difference density plots exhibit the effect well known from difference syntheses performed with high-order parameters, *i.e.* all bonding features have become more pronounced in comparison to Fig. 1. An improved separation of bond density and thermal smearing is also reflected in the peak heights of the charge accumulations on the bonds as given in Table 1. Thus, the core-refinement technique may be especially useful in obtaining more distinguishable bond density patterns in cases of restricted data sets. The inspection of the results of the rigid-bond test, however, indicates for the present study that the obtained thermal parameters of the cores have to be regarded with caution. It seems that the u_{ij}'s of the cores are generally somewhat too low as a consequence of high correlations with the valence electron clouds. Additionally, the statistical agreement of the mutual atomic vibrations is not better than for the SAM. In the case of NAH, Fig. 4(*a*) and Table 10 clearly show that the prominent difference in the z^2 of the S(2)–O(4) bond direction correlates with a too high residual charge distribution on that bond.

The described refinement tests were straightforward applications of the CM without tackling the correlation problem. High correlation coefficients were found between many variables and this may lead to unreasonable results in individual cases. A more systematic approach using reasonable constraints and following more sophisticated refinement paths may well yield improved results.

The multipole model (MM)

For the refinement with the multipole model we have used the least-squares program *LS-EXP* (Hirshfeld, 1971; Harel & Hirshfeld, 1975). In this model the electron density distribution of a stationary atomic arrangement is expressed as a superposition of spherical free-atom densities p_j^{at}, which are defined by the input scattering curves, plus a deformation density

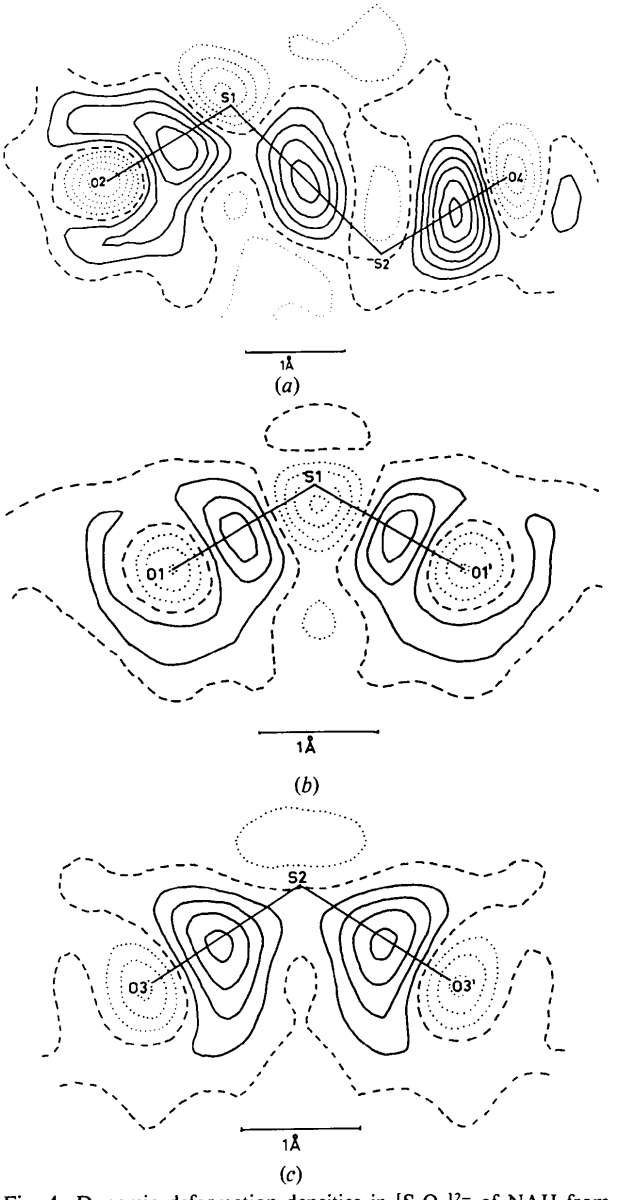

Fig. 4. Dynamic deformation densities in $[S_2O_6]^{2-}$ of NAH from (X–X_{core}) syntheses. Contours and planes are as in Fig. 1.

$d\rho$. $d\rho$ is approximated by localized linear combinations of atomic deformation functions ψ_{jl}:

$$\rho = \sum_{j=1}^{N} \left(\rho_j^{at} + \sum_{l=1}^{ML} c_{jl}\, \psi_{jl} \right).$$

More detailed descriptions of this model and its application have been described (Thomas, 1978; Kirfel, Gupta & Will, 1979). The final sets of atomic deformation functions describe then the static deformation densities of the atoms due to directed valence electron distributions. This means that all standard atomic parameters are expected to possess a minimum of bias introduced by bonding effects. In the present case, the complete set of deformation functions compatible with the atomic site symmetries comprised 198 members with 116 independently adjustable multipole coefficients c_{jl}. The number of deformation density functions allocated to each of the six unique atoms of $[S_2O_6]^{2-}$, as well as the imposed point symmetries, are compiled in Table 6. All multipole coefficients were started with zero values. The initial α values [α(S) = 12, α(O) = 8], which describe the radial decrease of the multipoles, were varied in separate cycles for NAH. The final values were 7·25 for S and 5·48 for O, which were then used for the refinement of NAD as well. Attempts to refine the subsidiary multipole coefficients along with the standard crystallographic parameters failed due to high correlation coefficients. Hence the refinements based on 1120 observations were in alternating cycles for the 116 subsidiary and 73 standard parameters. The final R values obtained were R ($R_{u.o.}$) = 0·0219 (0·0172) for NAD and 0·0181 (0·0129) for NAH. These values represent once more significant improvements compared to the preceding models. The relevant results of both refinements are given in Tables 9 and 10. The refined thermal parameters deserve attention. For both samples the mutual atomic vibrations agree in general within the limits of tolerance and the statistical agreement is the best of all models tested here. This result indicates the successful separation of the effects of thermal smearing from the covalent bonding by the multipole-expansion method.

Table 6. *Crystallographic and/or assumed point symmetries and numbers of allocated deformation functions for the multipole-expansion refinement of* $[S_2O_6]^{2-}$

	Site symmetry	Number of deformation functions
S(1)	*m*	22
S(2)	*m*	22
O(1)	*m*	22
O(2)	*mm*	14
O(3)	*m*	22
O(4)	*mm*	14
		Total 116

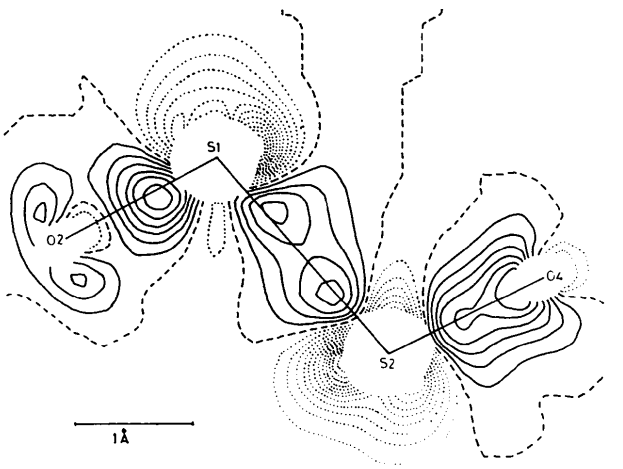

(*a*)

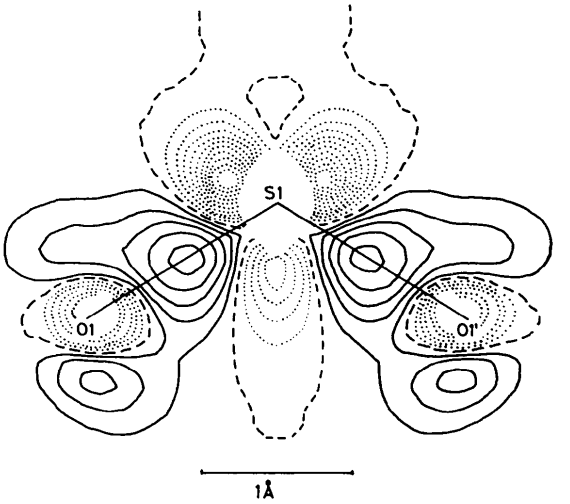

(*b*)

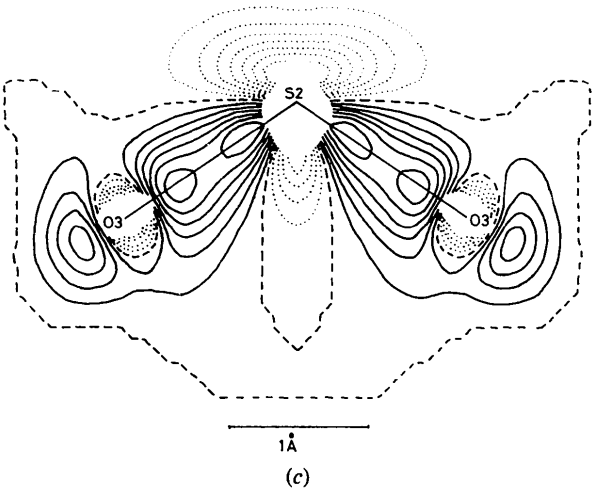

(*c*)

Fig. 5. Static deformation densities in $[S_2O_6]^{2-}$ of NAH from multipole-expansion refinement. Contours and planes are as in Fig. 1. Blank areas around atomic positions correspond to $\sigma(d\rho) \geq 0{\cdot}2$ e Å^{-3}.

Table 7. *Room-temperature mean-square vibrations* u_{ij} ($\times 10^4$ Å^2) *from multipole-expansion refinement (upper row NAH, lower row NAD)*

	u_{11}	u_{22}	u_{33}	u_{12}	u_{13}	u_{23}
S(1)	163 (1)	162 (1)	176 (1)	5 (1)		
	142 (1)	134 (2)	146 (1)	6 (1)		
S(2)	163 (1)	168 (1)	182 (1)	8 (1)		
	137 (1)	140 (2)	162 (2)	8 (1)		
O(1)	255 (4)	266 (4)	267 (4)	16 (3)	100 (3)	16 (3)
	240 (4)	236 (4)	231 (4)	11 (3)	95 (4)	31 (4)
O(2)	281 (6)	177 (5)	267 (5)	−27 (4)		
	260 (6)	138 (5)	225 (6)	−24 (5)		
O(3)	287 (4)	313 (4)	307 (4)	54 (3)	−130 (3)	−61 (4)
	253 (4)	278 (4)	282 (4)	56 (4)	−135 (4)	−56 (4)
O(4)	299 (6)	173 (5)	332 (6)	−28 (4)		
	259 (6)	142 (5)	289 (6)	−16 (5)		
O(5)	311 (5)	239 (4)	258 (4)	2 (4)	−7 (4)	−27 (3)
	286 (5)	207 (4)	235 (4)	3 (4)	−5 (4)	−26 (3)
Na	256 (2)	300 (2)	310 (2)	31 (2)	−36 (2)	−38 (2)
	228 (2)	272 (2)	287 (2)	33 (2)	−35 (2)	−41 (2)

Similar results have already been demonstrated for organic substances (Hirshfeld, 1976; Hansen & Coppens, 1978). Hence, if the rigid-bond postulate is correct, the thermal parameters from these last refinements can be regarded as the best obtainable values and to be of physical significance. They are therefore listed separately in Table 7 for both substances.

The positional parameters and the interatomic distances corroborate the results of the conventional refinement within the sums of the e.s.d.'s. An application of the riding correction provided by *LS-EXP* leads to distances in the anion which compare well with the corresponding results obtained from the BM. It seems, therefore, that the BM refinement technique provides a partial correction for thermal motion with respect to the bond distances.

Table 8. *Multipole coefficients* c_{jl} *exceeding* $3\sigma(c_{jl})$

	First neighbor	Second neighbor	N*	Direction	NAH	NAD
S(1)	S(2)	O(2)	3	110	2·00	1·70
				101	0·82	0·71
				111	−1·99	−1·72
			4	11α†	−0·33	
S(2)	S(1)	O(4)	2	1$\bar{1}$0	−0·57	
				011		0·60
			3	110	1·85	1·27
				101	0·90	0·79
				111	−1·93	−1·27
			4	100	0·46	0·56
O(1)	S(1)	S(2)	0		−0·23	−0·14
			2	101	0·26	
				110		0·34
O(3)	S(2)	S(1)	0		−0·20	
			2	1$\bar{1}$0	0·36	
				101		0·31
O(4)	S(2)	S(1)		101		0·45

* N = multipole order.
† $\alpha = \sqrt{2} - 1$.

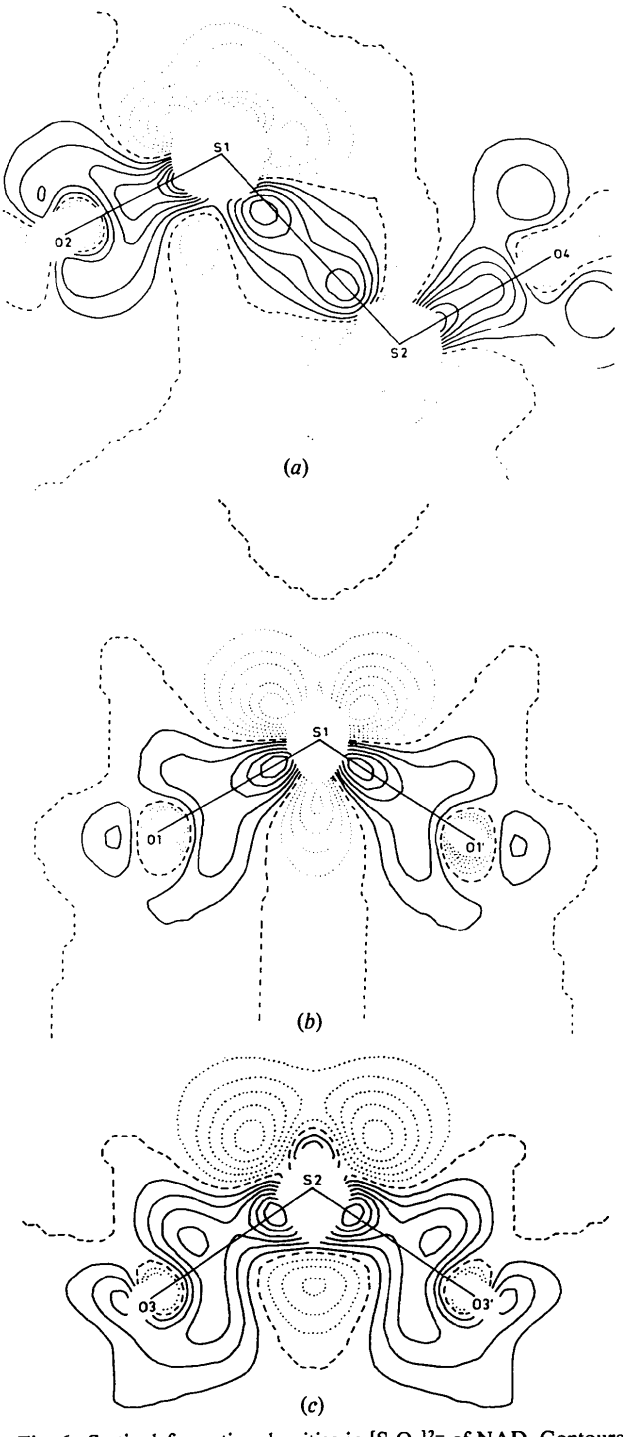

Fig. 6. Static deformation densities in $[S_2O_6]^{2-}$ of NAD. Contours and planes are as in Fig. 1.

The final multipole coefficients were then used to calculate static deformation density distributions in the interesting sections of $[S_2O_6]^{2-}$. The coefficients dominating the expansion of the static deformation density $[c_{jl} \geq 3\sigma(c_{jl})]$ are listed in Table 8. Plots of the

sections are depicted in Fig. 5 for NAH and in Fig. 6 for NAD. Fig. 7 contains as examples plots of the local e.s.d. of the deformation density. Accordingly the blank areas around the atomic positions in Figs. 5 and 6 correspond to $\sigma(d\rho) \geq 0{\cdot}2$ e Å^{-3}.

The similarity of the plots of both investigations is a measure of the reproducibility of $d\rho$. The features of the O–S–O sections compare well with the 78 K deformation densities in a sulfate group (Bats, 1977). Note the troughs in the deformation densities of the S atoms opposite the O–S–O valence angles. Lone-pair electron regions are indicated for the O atoms and in the O–S–O sections the charge density is asymmetric with respect to the S–O bonds, leading on average to a higher density inside the valence angles. Such a distribution may be interpreted in terms of an overlap of the $3d$ orbitals of the S with the $2p$ orbitals of the O atoms as proposed in the π-bond model (Cruickshank, 1961).

For some of the bonds, especially for the S–S bond, we find a splitting of the σ-bond charge accumulation resulting in two peaks which are separated by about 0·87 Å. This separation is well beyond the resolution limits of the data sets. Presently we cannot exclude that such findings reflect real deformation density features, but it seems more probable that the splitting results from an inadequate expansion of the deformation functions.

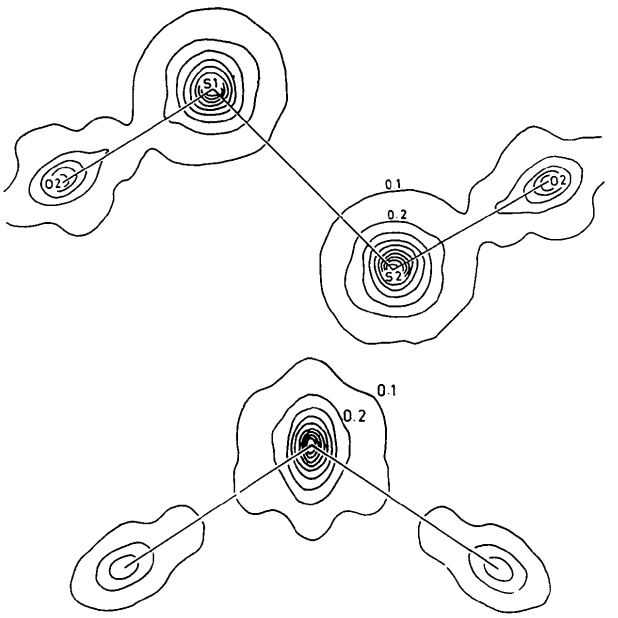

Fig. 7. E.s.d.'s of static deformation densities in $[S_2O_6]^{2-}$ of NAH. Contours are at intervals of 0·1 e Å^{-3}.

Pictorial representation of deformation densities

In order to obtain a better insight into the three-dimensional deformation density distribution within the $[S_2O_6]^{2-}$ anion we have depicted the static deformation density for fixed $d\rho$ values. This method has been employed already by Jorgenson & Salem (1973) (see also Smith, 1977). The contour lines for a constant $d\rho$ value were drawn in a sufficient number of equally spaced density sections. By a program-controlled uniform distortion and an origin shift for the sequence of layer plots, one obtains a graph which represents the envelope of the static deformation density at the required constant density value. Fig. 8 shows as an example the envelope of the positive deformation density inside $[S_2O_6]^{2-}$ of NAH at $d\rho = 0{\cdot}2$ e Å^{-3}. Only the multipole functions assigned to the S atoms were used for this plot. Thus the resulting density distribution displays merely the S contributions. The picture reveals clearly the charge accumulations by covalent bonding between the atoms due to the sp^3 hybridization of the S valence electrons.

Pursuing the idea of representing three-dimensional views of the redistribution of the valence electrons due

Table 9. *Agreement factors and interatomic distances* (Å) *in* $[S_2O_6]^{2-}$ (*upper values NAH, lower values NAD*)

	SAM	BM	CM	MM	Including riding correction
R ($R_{u.o.}$)	0·0255 (0·0198)	0·0224 (0·0162)	0·0201 (0·0139)	0·0181 (0·0129)	
	0·0278 (0·0229)	0·0257 (0·0210)	0·0239 (0·0191)	0·0219 (0·0172)	
GOF	0·64	0·56	0·52	0·85	
	0·65	0·62	0·59	0·80	
S(1)–S(2)	2·140 (1)	2·141 (1)	2·142 (1)	2·140 (1)	2·140
	2·142 (1)	2·142 (1)	2·142 (1)	2·141 (1)	2·142
S(1)–O(1)	1·449 (1)	1·458 (2)	1·449 (2)	1·450 (1)	1·459
	1·450 (1)	1·457 (3)	1·452 (1)	1·450 (1)	1·460
S(1)–O(2)	1·455 (2)	1·461 (2)	1·458 (3)	1·455 (2)	1·462
	1·456 (2)	1·461 (3)	1·460 (3)	1·455 (2)	1·462
S(2)–O(3)	1·449 (1)	1·458 (2)	1·456 (2)	1·450 (1)	1·463
	1·450 (1)	1·454 (3)	1·453 (2)	1·450 (1)	1·463
S(2)–O(4)	1·452 (2)	1·463 (3)	1·460 (3)	1·457 (2)	1·463
	1·452 (2)	1·458 (3)	1·459 (3)	1·453 (1)	1·461

Table 10. *Mutual atomic vibrations* $z^2_{A,B}$ *and* $z^2_{B,A}$ ($\times 10^4$ Å^2) (*upper values NAH, lower values NAD*)

	SAM		BM		CM		MM	
S(1)–S(2)	158	155	160	156	152	149	160	159
	135	139	133	129	125	123	132	131
S(1)–O(1)	174	181	171	169	162	152	175	172
	148	156	148	142	137	141	146	145
S(1)–O(2)	167	171	168	137	153	149	169	178
	144	150	138	135	135	129	141	145
S(2)–O(3)	187	207	186	188	180	168	182	176
	161	161	158	155	149	135	157	154
S(2)–O(4)	173	182	172	145	164	143	175	173
	148	154	147	131	139	134	146	150
r.m.s. (Δz^2)	10·5		18·8		11·9		5·1	
	5·4		8·1		6·2		2·9	

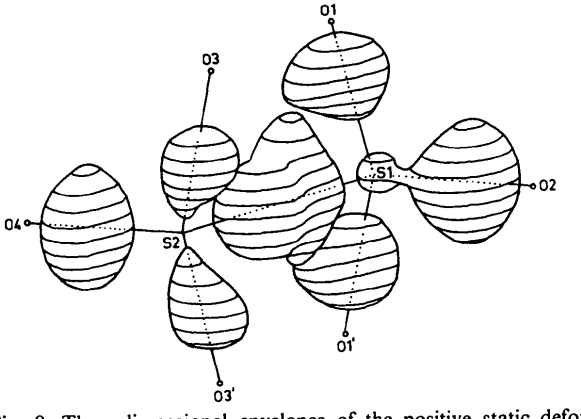

Fig. 8. Three-dimensional envelopes of the positive static deformation density at 0·2 e Å^{-3} calculated from refined S(1), S(2) multipole coefficients of NAH.

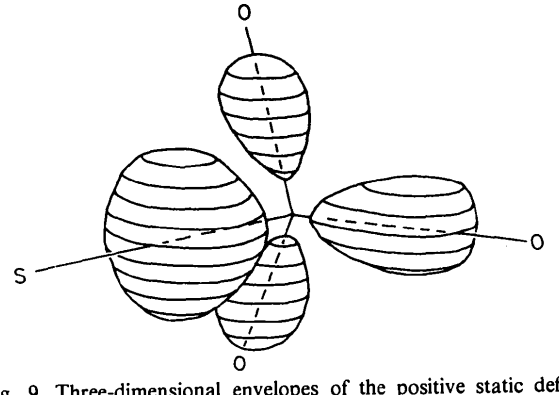

Fig. 9. Three-dimensional envelopes of the positive static deformation density at 0·1 e Å^{-3} calculated from the averaged S multipole coefficients of NAH and NAD.

to covalent bonding, we have tried to reduce the relatively large uncertainties in the multipole expansion of individual atoms by chemical averaging. S(1) and S(2) of both NAH and NAD were regarded in first-order approximation as chemically equivalent. The chemical averaging was performed by calculation of weighted

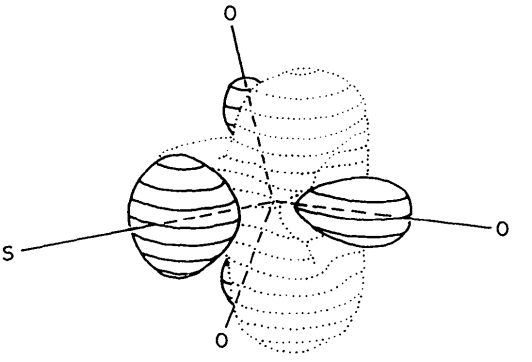

Fig. 10. Three-dimensional envelopes of the positive and negative (dotted) deformation density at ±0·2 e Å^{-3} calculated from the averaged S multipole coefficients of NAH and NAD.

means of the corresponding multipole coefficients of the four S atoms. These mean values served for the calculation of the static deformation density of a mean S atom surrounded by an environment of one S and three O atoms in tetrahedral coordination. Fig. 9 shows the three-dimensional envelope at constant $d\rho$ = 0·1 e Å^{-3} of such a S atom. The positive and negative envelopes at +0·2 and −0·2 e Å^{-3} are depicted in Fig. 10. Both figures show in a very instructive way the effects of bonding, *e.g.* the redistribution of the formerly spherical valence electron density distribution of the free atom.

This kind of plot still deals with the deformation density. For comparison we have calculated also a superposition of the total spherical density of the free S atom as obtainable from the Fourier transformation of

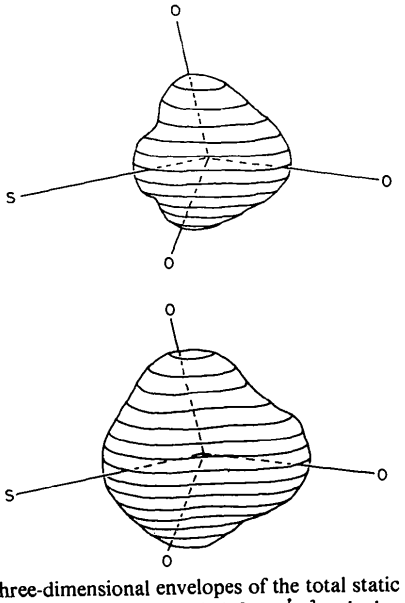

Fig. 11. Three-dimensional envelopes of the total static density of S in $[S_2O_6]^{2-}$ at 1·5 (top) and 1·0 e Å^{-3} calculated from the averaged S multipole coefficients and the S scattering-factor curve.

the scattering-factor curve and the static deformation density:

$$\rho(\mathbf{r})^{at}_{bonded} = \rho(\mathbf{r})^{at}_{free} + d\rho(\mathbf{r}).$$

Fig. 11 shows the envelopes of the total static electron density distribution of the above-defined S atom at $\rho =$ 1·0 and $\rho =$ 1·5 e Å^{-3}. This total distribution gives a true impression of the bonding effects and the graphs show that the deformation of the electron shell is of considerable magnitude. Although the preparation of such graphs is time-consuming, we feel that in selected cases they may serve better than conventional two-dimensional sections for the presentation of bonding effects on single atoms or atomic arrangements.

Conclusions

(1) The four models applied for the refinement of the electron density distribution in $[S_2O_6]^{2-}$ yielded improved descriptions of the density ordered with increasing degree of complexity of the model. Thus they prove to be useful in assessing the evaluation of deformation densities in molecular fragments containing second-row elements such as S. The improvement of the agreement factors is not artificial, *i.e.* merely due to the increased number of variable parameters. This can be seen from Fig. 12 which contains significance points for all refinements calculated from Hamilton tests. The curves represent 0·005 confidence levels for $n - m = 500$ and $n - m = 1000$ respectively. Since both data sets consist of 1120 observations, the significance points are all well beyond these levels. According to Fig. 12 we find the multipole-expansion model to be the most adequate for the analytical description of the observed density, and hence we conclude that the parameters resulting from the MM refinement are least biased by bonding effects (compare rigid-bond test).

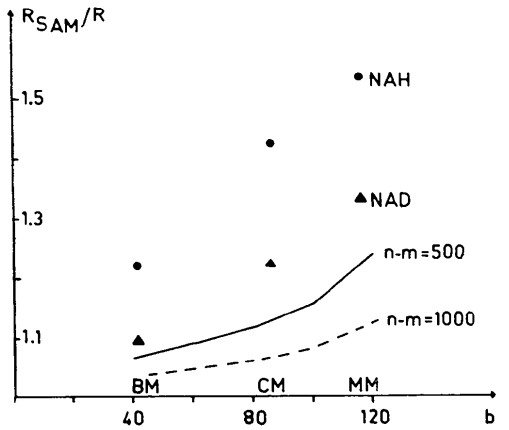

Fig. 12. Significance points of NAH and NAD refinements with $n = 1120$ observations. Curves represent $\alpha = 0{\cdot}005$ confidence levels for selected $n - m$ differences. b = number of additional variables compared to conventional refinement; m = total number of variables.

(2) The corresponding results of the individual refinements of both data sets agree generally within the limits of tolerance. This is not true for the absolute values of the vibrational parameters of NAH and NAD, though it is the case for their relative distributions. As already discussed in part I, we do not have a satisfactory explanation for these differences. The calculated deformation densities (dynamic and static) show qualitatively agreeing features of bonding densities, and since the data sets have been collected under different experimental conditions, systematic experimental errors do not seem to be of importance. The results obtained are dependent on the model rather than on the experiment. Hence a discussion of the models and of the chemical bonding in the anion can be based on qualitatively reproduced results from two independent measurements.

(3) The ionic model corroborates well the twofold negative charge character of the S_2O_6 anion. It leads to the simple idea of neutral S and O atoms carrying the two excess electrons uniformly distributed over all atoms.

(4) The bond model reveals the covalent bonding between the atoms. σ-bond charge-cloud accumulations of considerable density peak heights and at physically reasonable positions can be refined to establish the degree of covalent bonding and eventually the nature of the atomic orbitals involved. The anion charge is again reproduced within the limits of tolerance.

(5) The core model is useful in evaluating atomic parameters less biased by bonding effects, which are desirable for *X–X* syntheses. The resulting dynamic deformation densities are much more pronounced than those from the conventional refinements and thus imply a better separation of bonding effects and thermal smearing. The present investigations show that the method works for restricted data sets. However, the correlation problem is serious and therefore the refinement must be performed with great care.

(6) The multipole model, yielding the most promising results, is easy to apply and leads to static deformation densities which may be compared with *ab initio* calculations. The analytical description of the deformation density offers the possibility of considering individual atomic deformations in two- and three-dimensional representation. Again there is a considerable correlation problem, which may sometimes lead to unreasonable results. We feel that the refinement strategy is of great importance and must be studied in more detail. This applies especially for the refinement of the input shapes of the deformation functions.

(7) Considering all results, the bonding in $[S_2O_6]^{2-}$ is much more of covalent nature than widely assumed. S–S and S–O σ bonds are clearly established; S(3*d*)

and O(2*p*) interaction (Cruickshank, 1961) is indicated by asymmetric density distributions with respect to the S–O bond directions. The anion behaves like a rigid body and can be treated as a charged molecular fragment. Chemical assignments of charges such as S^{4+} and O^{2-} are not adequate and should not be used for refinement purposes. Conventional refinements of similar anions promise better agreement with observed densities if started with neutral atoms.

This work has received the support of the Deutsche Forschungsgemeinschaft, which is gratefully acknowledged.

References

BATS, J. W. (1977). *Acta Cryst.* B**33**, 2035–2041.

BERTHOLD, I. & WEISS, A. (1967). *Z. Naturforsch. Teil A*, **22**, 1440–1451.

COPPENS, P. (1971). *Acta Cryst.* B**27**, 1931–1938.

CRUICKSHANK, D. W. J. (1961). *J. Chem. Soc.* pp. 5486–5504.

HANSEN, N. K. & COPPENS, P. (1978). *Acta Cryst.* A**34**, 909–921.

HAREL, M. & HIRSHFELD, F. L. (1975). *Acta Cryst.* B**31**, 162–172.

HELLNER, E. (1977). *Acta Cryst.* B**33**, 3813–3816.

HIRSHFELD, F. L. (1971). *Acta Cryst.* B**27**, 769–781.

HIRSHFELD, F. L. (1976). *Acta Cryst.* A**32**, 239–244.

International Tables for X-ray Crystallography (1974). Vol. IV. Birmingham: Kynoch Press.

JOHNSON, C. K. (1965). *ORTEP*. Report ORNL-3794. Oak Ridge National Laboratory, Tennessee.

JORGENSON, W. L. & SALEM, L. (1973). *The Organic Chemist's Book of Orbitals*. New York: Academic Press.

KIRFEL, A., GUPTA, A. & WILL, G. (1979). *Acta Cryst.* B**35**, 1052–1059.

KIRFEL, A., WILL, G. & WEISS, A. (1980). *Acta Cryst.* B**36**, 223–228.

KÜTOGLU, A. & HELLNER, E. (1978). *Acta Cryst.* B**34**, 1617–1623.

KUTOGLU, A. & SCHERINGER, C. (1979). *Acta Cryst.* A**35**, 458–462.

MULLEN, D. & HELLNER, E. (1977). *Acta Cryst.* B**33**, 3816–3822.

NOVER, G. (1977). Thesis, Mineralogisches Institut der Universität Bonn.

PAULING, L. (1960). *The Nature of the Chemical Bond*, 3rd ed. Ithaca: Cornell Univ. Press.

SMITH, V. H. (1977). *Phys. Scr.* **15**, 147–162.

STEVENS, E. D. (1978). *Acta Cryst.* B**34**, 544–551.

STEVENS, E. D. & HOPE, H. (1975). *Acta Cryst.* A**31**, 494–498.

THOMAS, J. O. (1978). *Acta Cryst.* A**34**, 819–823.

WILL, G., FRAZER, B. C., SHIRANE, G. & COX, D. E. (1965). *Acta Cryst.* **19**, 854–857.

Acta Cryst. (1980). B**36**, 523–526

Convergent-Beam Electron Diffraction Symmetry from a Disordered Structure (Ce, Ta) Ta_6O_{19}

BY A. W. S. JOHNSON

CSIRO Division of Chemical Physics, PO Box 160, *Clayton, Victoria* 3168, *Australia*

AND B. M. GATEHOUSE

Department of Chemistry, Monash University, Clayton, Victoria 3168, *Australia*

(*Received* 6 *July* 1979; *accepted* 4 *September* 1979)

Abstract

The space group of (Ce,Ta)Ta_6O_{19} is shown by convergent-beam diffraction to be $P\bar{6}c2$ and not $P6_3/mcm$ as previously reported by X-ray diffraction. The X-ray structure, however, is essentially correct, the major change being the ordering of the Ce and Ta atoms in the special positions $\frac{1}{3}, \frac{2}{3}$ and $\frac{2}{3}, \frac{1}{3}$ in strings parallel to the *c* axis with Ce at $\frac{1}{3}, \frac{2}{3}$ and Ta at $\frac{2}{3}, \frac{1}{3}$. Occasional interchanging of these strings would explain the space group observed in the X-ray determination.

Introduction

This investigation of cerium tantalate by convergent-beam electron diffraction was undertaken with three aims in mind. These were to determine the space group of a structure which X-ray refinement had shown to possess a random distribution of some atoms, to further structural knowledge of cerium tantalate, and to extend experience in interpreting convergent-beam electron diffraction (CBED) patterns from unit cells with long axes. The work emphasizes the need to distinguish

0567-7408/80/030523-04$01.00